

Selective C(sp²)-H Amination Catalyzed by High-Valent Cobalt(III)/(IV)-bpy Complex Immobilized on Silica Nanoparticles

Yulia Budnikova,^{*[a]} Olga Bochkova,^[a] Mikhail Khrizanforov,^[a] Irek Nizameev,^[a] Kirill Kholin,^[a] Tatyana Gryaznova,^[a] Artem Laskin,^[b] Yulia Dudkina,^[a] Sofia Strekalova,^[a] Svetlana Fedorenko,^[a] Aleksandr Kononov,^[a] and Asia Mustafina^[a]

High-valent cobalt^{IV}-bpy complex stabilized in silica matrix was detected as catalytically active form and intermediate in cobalt-mediated oxidative C–H/NH cross-coupling reaction. These Co^{IV} species prepared by electrooxidation of Co^{III}(bpy)₃-doped silica nanoparticles (SNs) at relatively low anodic potentials have demonstrated high catalytic activity. Both size and architecture of the SNs are highlighted as the factors beyond the complex structure affecting its oxidation potential and catalytic efficiency. The factors have been optimized for the catalyst with high efficiency, easy separation and reusability for 7 times at

least. The optimal nanocatalyst (1 mol%) provides 100% conversion of reactants in a single step of ligand-directed coupling of H₂NTs with arenes under electrochemical regeneration conditions. The results emphasize both synthetic route for efficient embedding of Co^{III}(bpy)₃ into silica support and the electrochemical generation of Co^{IV} complexes as a facile route for developing the efficient nanocatalyst of oxidative functionalization. The observed reactivity has the potential in development of Co-catalyzed coupling reactions.

1. Introduction

The developing an efficient, selective and environmentally friendly catalyst system is of paramount importance, especially for the highly sought-after reactions of atom-economy direct C–H functionalization. First row transition metals are promising catalysts due to both great diversities in coordination geometry, and multiple spin states that help in the manipulation of the electronic structure of the resulting complex as required during different steps of the catalysis. Although numerous catalytic systems based on transition metal salts or complexes have been developed for this purpose,^[1] in most of them separation of the catalyst from the homogeneous reaction mixture and its subsequent recovery in active form is cumbersome. Thus, considerable efforts are directed towards the development of heterogeneous or nanoheterogeneous catalysts for organic reactions^[2] but there are not so many successful examples for C–H activation and functionalization, and no reports on C–H amination. In this regard, encapsulation and/or immobilization of homogeneous catalysts on the surface and in the cavities of suitable supports such as zeolites and structurally tailored sol-gel materials have received considerable attention in recent times.^[3] Moreover, in addition to the easily product separation,

catalyst recovery and reusability, the transfer of catalytically active transition metal complexes from homogeneous to nano-heterogeneous forms can often improve an activity and selectivity of the catalyst.^[3] Catalytic systems that work under oxidative conditions would allow for a broader scope of applications in C–H bond functionalization. A more recent trend is the use of earth-abundant and inexpensive first-row metals, such as Cu^{II},^[4] Ni^{II},^[4a,5] and Co^{II/III,IV,5,6} as opposed to precious metals such as Pd, Ir, Rh. Currently, there are mainly two types of Co^{III} catalysts for CH activation/functionalization reactions. First type,^[6h] is characterized by bearing a cyclopentadienyl (Cp) type ligand^[1e–l,6]; the other type,^[6i] has no Cp type ligand, but the existence of N,N'- or N,O-bidentate directing groups in the substrates is indispensable in most cases. The catalysis is based on Co(OAc)₂ as the Co^{II} precatalyst which is oxidized to Co^{III} coordinated with N,N'- or N,O-bidentate directing groups under the action of chemical or electrochemical oxidants.

Moreover, Co^{IV} is still a rare oxidation state, and the isolated, well characterized examples that are stable at room or even low temperature are few.^[7] Terminal cobalt(IV)-oxo (Co^{IV}–O) species and mixed-valence, tetranuclear cobalt(III, IV) complexes have been implicated as key intermediates in some cobalt-mediated oxidation reactions, mainly for the oxidation of water or alcohols^[7]. Recently, three-coordinate (IMes)Co^{IV}(NDipp)₂ and [(IMes)Co^V(NDipp)₂][BARF₄] bis-imido complexes, where IMes = 1,3-bis(1',3',5'-trimethylphenyl)imidazol-2-ylidene, Dipp = 2,6-diisopropylphenyl, have been reported from the Deng group.^[8] Interestingly, the imido-bound Co^{IV} (S = 1/2) undergoes intramolecular C–H activation of a benzylic C–H bond from the IMes ligand (with a subsequent C–N forming step). Co^{IV} complexes as a platform for oxidative C–H functionalization including C–H/NH coupling are practically not studied, although there are

[a] Prof. Dr. Y. Budnikova, Dr. O. Bochkova, Dr. M. Khrizanforov, Dr. I. Nizameev, Dr. K. Kholin, Dr. T. Gryaznova, Y. Dudkina, Dr. S. Strekalova, Dr. S. Fedorenko, A. Kononov, Prof. Dr. A. Mustafina
Arbuzov Institute of Organic and Physical Chemistry
FRC Kazan Scientific Center, Russian Academy of Sciences
420088, Arbuzov str. 8, Kazan (Russian Federation)
E-mail: yulia@iopc.ru

[b] A. Laskin
Kazan Federal University
Kremlevskaya str. 29/1, Kazan, 420008 (Russian Federation)

many cobalt-catalyzed reactions.^[1,6] This is due to the difficulty in obtaining and stabilization of Co^{IV}, since the highly oxidized cobalt derivatives are very sensitive to moisture, light, and, as a rule, have a high reactivity. Thus, strong oxidizing conditions (PhIO, Na₂S₂O₈ or irradiating in the presence of [Ru^{II}(bpy)₃]^[7g] are required to obtain Co^{IV} complexes with their further stabilization by complex methods. For example, [Co^{IV}(O)(M⁺)⁽ⁿ⁺²⁾⁺ intermediates are stabilized by complicated ligands^[8 and refs therein] or redox-inactive Lewis acidic metal ion (e.g., Sc³⁺ ion) (M⁺ = Sc³⁺, Ce³⁺, Y³⁺, and Zn²⁺)^[7e,d] which can interfere with the Co^{IV} under their use in catalysis.

It is worth noting that no reliable evidence for the generation of Co^{IV} species as part of a catalytic cycle in C–H transformations has been provided thus so far. However, the search for new efficient reusable catalytic systems based on high-valent cobalt compounds is extremely in demand and relevance. An attractive goal is to obtain cobalt derivatives in highest degrees of oxidation, stabilized by specific environment so that they will be highly effective in catalytic reactions and at the same time easy to handle and separate from the reaction mixture, suitable for reactivation and regeneration. It is very important for successful catalysis to find a suitable inner-sphere cobalt environment and specific external conditions, such as the nature of the matrix in which the cobalt species are immersed, size and architecture of a composite nanomaterial.

Transparency and stability of silica matrix, as well as an easy size limitation providing a synthesis of nanosized silica particles are the reasons for their wide application as a platform for embedding of different metal-based species. The embedding of the complexes into silica nanoparticles enables to facilitate their applicability in catalysis and biosensing due to greater reusability and smaller toxicity. Literature data introduce some synthetic tools to vary the main characteristics of composite silica nanoparticles, including their size, uploading efficiency and the morphology.^[9] The present work introduces the optimal synthetic techniques for embedding of Co^{III} complexes into silica nanoparticles as the route to stabilize the Co^{IV} complex forms produced by the electrochemical oxidation. The Co^{III} (bpy)₃ complexes due to their kinetic inertness are rather promising candidates for embedding into silica nanoparticles, although the previously documented redox data on Co(bpy)_nX_n in solutions were always limited to Co^{(III)/(II)/(I)/(0)} transfers or even Co⁽⁰⁾^[10] but never Co^{III/IV} transition, since it was impossible to generate Co^{IV}-bpy in the homogeneous conditions.

It is worth noting that both synthetic routes for embedding of the tris-bipyridine complexes into silica nanoparticles and their electrochemical behavior are documented in greater extent for Ru^{II}^[11] versus Co^{III}^[12] complexes. For the best of our knowledge there are very few articles on synthesis and electrochemical behavior of silica nanoparticles doped with Co^{III}(bpy)₃ complexes.^[12a] Moreover, an effect of the size and morphology of Co^{III}(bpy)₃-doped silica nanoparticles on their electrochemical behavior is rather poor if any documented in literature. Thus, the present work is aimed at highlighting facile synthetic route for efficient uploading of differently sized (4.5–140 nm) silica nanoparticles by Co^{III}(bpy)₃ complexes. Correlation of the uploading efficiency and the size of the composite silica

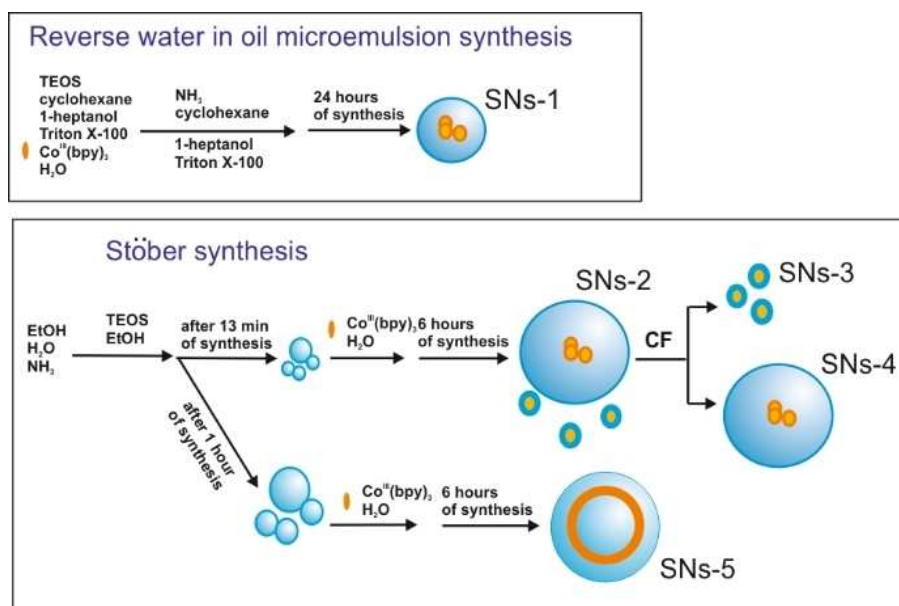
nanoparticles with synthetic conditions are also introduced herein along with correlation of their electrochemical behavior with the morphology and the size of the composite nanoparticles. The present study considers the inclusion of the complexes into silica confinement as the convenient way to solve the problem of stabilization of the cobalt complexes in high oxidation state, which enables to introduce the composite silica nanoparticles as very interesting platform for oxidative catalytic reactions. The Co^{IV} complex will be produced electrochemically by oxidation of Co^{III}(bpy)₃ within a silica confinement, so as to obtain stable nanoparticulate systems, however, active in C–H bond substitution reactions, namely aromatic CH amination.

2. Results and Discussion

2.1. Co^{III}(bpy)₃-doped Silica Nanoparticles Synthesis

Presentation of the synthesized composite silica nanoparticles is worth proceeding by discussion of the main synthetic routes applied for these purposes. Two main synthetic procedures are worth noting. The first procedure is based on adsorption of metal ions or complexes at a silica surface which, in turn, is driven by coordinative and/or electrostatic interactions. The former interactions derive from the presence of Si–OH groups at a silica surface which makes probable inner-sphere coordination of metal ions or complexes *via* Si–O[−] groups. This tendency was previously reported for different metal ions and complexes.^[13] It was, in particular, demonstrated, that the coordination *via* Si–O[−] groups occurs even under the adsorption of Co^{II}(en)₃ resulting in the ternary complex formation accompanied by a partial dechelation of the complex.^[13a] The second way of the embedding is the so-called doping or uploading procedure based on the inclusion of metal complexes into silica confinement when the growth of silica nanoparticles occurs in the presence of metal complexes.^[2c,9c–e] The inclusion of the complexes in the silica nanoparticles results from both adsorption of the complexes onto silica surface and precipitation of the complexes in the silica confinement. The adsorption, in turn, can result from inner-sphere coordination *via* Si–O[−] groups and/or outer-sphere electrostatic attraction between complex cations and negatively charged silica surface. Some of the previous reports indicate the inner-sphere coordination accompanied by the dechelation of labile transition complexes including Ni^{II}(bpy)₃ as a consequence of the doping procedure.^[2c,9d] The embedding of kinetically inert complexes Ru^{II}(bpy)₃ and Co^{III}(bpy)₃ exemplify rather specific case, since their inclusion into silica confinement is mainly based on electrostatic attraction, Van der Waals interactions and physical absorption without detectable changes in the inner-sphere environment of the metal ions.^[11,12a]

The size of silica nanoparticles can be controlled by variation of the synthetic conditions, such as a nature of surfactant and/or solvent, concentrations of the key synthetic components, as well as their concentration ratios.^[9] The uploading efficiency is mainly controlled by concentration of



Scheme 1. Schematic representation of different techniques for synthesis of $\text{Co}^{\text{III}}(\text{bpy})_3$ -doped silica nanoparticles. CF means centrifugation stage.

the added complex and its phase state (as true solution or colloids) in the synthetic mixture,^[14] since silica coating of colloidal nanoparticles can be the alternative process to adsorption of the molecular complexes onto silica surface under the growth of composite silica nanoparticles. This can be a reason for greater polydispersity of the composite nanoparticles. Thus, any precipitation of metal complexes in the synthetic mixture greatly influences a size uniformity of silica nanoparticles. The problem of convenient solubility of the dopant can be solved by both proper choice of synthetic procedure and its modification. In particular, silica spheres grow within aqueous nano-droplets of inverse micelles in the framework of water-in-oil microemulsion technique.^[9a,e] Thus, the latter is convenient for efficient uploading of silica spheres by water soluble metal complexes, while Stöber procedure is more convenient for the complexes with enough solubility in alcohol.^[9b-d]

Indeed, the synthesis by means of water-in-oil microemulsion procedure schematically illustrated by Scheme 1 results in the uploading of $\text{Co}^{\text{III}}(\text{bpy})_3$ complexes into universe in size 50 ± 5 nm silica spheres (Figure 1, A), which is evident from the content of Co in the composite nanoparticles. The size, content and colloid characteristics of the composite nanoparticles designated as SNS-1 are in the Table 1. Good water solubility of $\text{Co}^{\text{III}}(\text{bpy})_3$ complexes is the prerequisite for the result.

Stöber procedure is another versatile synthetic framework widely applied for producing composite SNS.^[2c,9d] The low solubility of $\text{Co}^{\text{III}}(\text{bpy})_3$ complexes in alcohol is the reason for their addition into the alcohol-based synthetic mixture in a form of the aqueous aliquotes which is also illustrated by the Scheme 1. However, the solubility of $\text{Co}^{\text{III}}(\text{bpy})_3$ complex in the synthetic solutions is still inconvenient which is manifested by

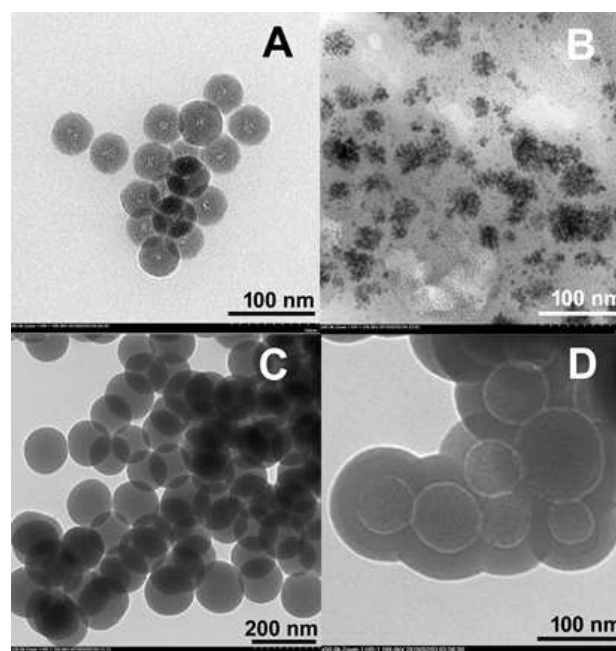


Figure 1. TEM images of different types of silica nanoparticles doped with $\text{Co}^{\text{III}}(\text{bpy})_3$: SNS-1 (A), SNS-3 (B), SNS-4 (C), SNS-5 (D).

the appearance of a turbidity under its addition to the synthetic mixture. The TEM analysis of the separated silica nanoparticles reveals significant polydispersity. In particular, silica nanoparticles with two different sizes both ~ 5 and above 100 nm (SNS-2) were separated from the synthetic mixture when the aqueous solution of $\text{Co}^{\text{III}}(\text{bpy})_3$ was added at the beginning of the synthesis. The separation of the differently sized nanoparticles is based on the quicker sedimentation of the smaller nanoparticles in the aqueous solutions which enables to

Table 1. Diameter of $[\text{Co}^{\text{III}}(\text{bpy})_3]@\text{SiO}_2$ by TEM (d), their Si:Co Molar ratio by ICP-OES technique, Peak means of Size distribution by number ($n=3$), Polydispersity index (PDI) and zeta potential values (ζ) ($\text{SD}=3\text{ mV}$, $n=3$) depending on type of silica nanoparticles ($C=0.2\text{ g L}^{-1}$) in water.

Sample	d [nm]	Si:Co molar ratio	Peak means, nm	PDI	ζ [mV]
SNs-1	50 ± 5	100:0.726	144 ± 1	0.105	-33
SNs-2	-	100:0.368	167 ± 3	0.325	-50
SNs-3	4.5 ± 1	100:0.659	204 ± 32 -85%, 874 ± 247 -15%	0.495	-15
SNs-4	140 ± 9	100:0.098	170 ± 2	0.028	-51
SNs-5	116 ± 19	100:0.427	151 ± 25 -99.6%, 1513 ± 274 -0.4%	0.755	-41

separate small ($\sim 5\text{ nm}$) and large ($\sim 140\text{ nm}$) silica spheres from each other. The TEM images of the small and large composite nanoparticles designated as SNs-3 and SNs-4 are presented in panels B and C of Figure 1, while SNs-2 are the mixture of SNs-3 and SNs-4. Synthetic conditions were modified to avoid the polydispersity of the nanoparticles. For this reason, the complexes were added after some time from the synthesis beginning in order to avoid the precipitation of the complexes by their adsorption onto silica seeds. It is known that one hour is enough time duration for the preliminary synthesis of silica spheres, while their growth is incomplete.^[2c,9d] The addition of the aqueous solution of $\text{Co}^{\text{III}}(\text{bpy})_3$ after one hour from the synthesis beginning results in the growth of rather universe in size ($120 \pm 10\text{ nm}$) silica spheres designated as SNs-5 (Figure 1). The insignificant degradation of $\text{Co}^{\text{III}}(\text{bpy})_3$ complexes within the synthesis and their efficient transfer from the synthetic solutions to the silica nanoparticles is confirmed by the analysis of the supernatant synthetic solutions (Figure S1 in SI).

Analysis of the nanoparticles in their aqueous colloids by means of both ICP-OES and DLS techniques reveals greater tendency of the smaller nanoparticles to aggregate due to the charge neutralization, in turn, arisen from their greater uploading by $\text{Co}^{\text{III}}(\text{bpy})_3$ complexes which are both positively charged and tend to locate close to an interfacial zone due to the small nanoparticulate size. The evaluated by ICP-OES technique Si:Co molar ratios for the differently sized (5 and 140 nm) composite nanoparticles indicate the greater content of Co in the smaller nanoparticles (Table 1). *Vice versa*, the greater sized silica spheres SNs-4 exhibit greater colloid stability due to high negative charge of their silica surface correlating with their poor uploading by $\text{Co}^{\text{III}}(\text{bpy})_3$ complexes. The size ($\sim 120 \pm 10\text{ nm}$) of SNs-5 is characterized by rather high content of Co measured by ICP-OES technique (Table 1). The TEM images of the SNs-5 reveal the bright rings inside the silica spheres which can be attributed to included $\text{Co}^{\text{III}}(\text{bpy})_3$ complexes. Thus, the aggregation is the most for the smallest SNs-3 and detectable for SNs-1 (Table 1). The tendency correlates with the electrokinetic potential values of the nanoparticles which, in turn, are greatly affected by the concentration of the complexes in the interfacial zones of the silica spheres. The results point to some silica surface charge neutralization due to the presence of the complex cations at the silica/water interface, although the

leaching of the complexes from the nanoparticles is rather low (Figure S2 in SI).

The Si:Co ratios of the composite nanoparticles SNs-1(2–5) collected in Table 1 indicate the greatest content of $\text{Co}^{\text{III}}(\text{bpy})_3$ in SNs-1 obtained by the microemulsion procedure. The EDX measurements were performed for SNs-1 and SNs-5 to get the additional confirmation of the inclusion of $\text{Co}^{\text{III}}(\text{bpy})_3$ into the silica spheres (Figure S3 in SI). The Co-content in SNs-2(3–5) synthesized through the Stöber procedure is somewhat smaller than that for SNs-1 and greatly depends on the synthetic mode. In particular, the Co-content is the greatest for the smallest nanoparticles SNs-3 among SNs-2(3–5). This confirms the above mentioned assumption that their formation results from the silica coating of the nano-sized precipitates of $\text{Co}^{\text{III}}(\text{bpy})_3$, when the latter is added at the beginning of the synthesis. However, the precipitation doesn't exclude the growth of the greater sized silica spheres SNs-4 with the smallest Co-content, since the equilibrium concentration of $\text{Co}^{\text{III}}(\text{bpy})_3$ in the synthetic mixture is significantly decreased by the precipitation. The optimal result from the viewpoints of the size university and the Si:Co ratio was obtained for SNs-5 synthesized when $\text{Co}^{\text{III}}(\text{bpy})_3$ was added 60 minutes after the synthesis beginning. It is worth noting that 60 minutes is enough time for the growth of the silica seeds^[9c,d] with an active surfaces open for the adsorption of $\text{Co}^{\text{III}}(\text{bpy})_3$. This fact along with the lower concentrations of TEOS and ammonia in the synthetic mixture can be the reason for the insignificant precipitation of the added complex. The adsorption of the complex onto the silica seeds, nevertheless, doesn't prevent further silica coating which results in the Co(III)-doped silica nanoparticles with the better university in size. In the assumption that the bright rings in the TEM images of SNs-5 (Figure 1) indicate the layers of the doped complex, the sizes of silica seeds exceed 50–100 nm after one hour of the synthesis, while the thickness of the further silica coating of the adsorbed complex is about 35 nm.

Transparency of a silica matrix provides the opportunity to reveal the spectral behavior of the complexes. Thus, the complexes inside the nanoparticles are manifested by the spectral pattern (two absorption bands) similar with that for $\text{Co}^{\text{III}}(\text{bpy})_3$ in acetonitrile solutions (Figure 2). However, both change in the intensity ratio of the bands and their shifting to longer wavelengths versus the wavelengths of the "free" $\text{Co}^{\text{III}}(\text{bpy})_3$ can be considered as "rigidochromism".^[15]

3. Electrochemical and ESR Studies

The redox behavior of $\text{Co}^{\text{III}}(\text{bpy})_3$ within SNs-1(2–5) was examined by cyclic voltammetry (CV) using the carbon paste electrode (CPE) based on the phosphonium salt. This technique was previously reported as very efficient route for analyzing redox properties of insoluble or low-soluble and nanoparticulate complexes in a wide range of potentials.^[2c,16] The measured CVs are presented in Figure 3. The electrochemical characteristics of the nanoparticulate complexes are collected in Table 2 along with the similar values for the initial $[\text{Co}(\text{bpy})_3](\text{ClO}_4)_3$ complex measured in CH_3CN solution for the comparison.

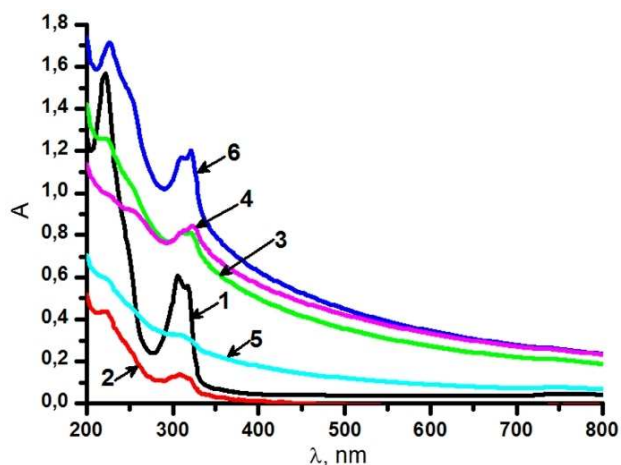


Figure 2. UV-vis absorption spectra of $\text{Co}(\text{bpy})_3(\text{ClO}_4)_3$ solution ($C = 1.67 \cdot 10^{-5} \text{ M}$) (1) and SNs dispersions ($C = 0.2 \text{ g L}^{-1}$) in acetonitrile: SNs-1 (2), SNs-2 (3), SNs-3 (4), SNs-4 (5), SNs-5 (6).

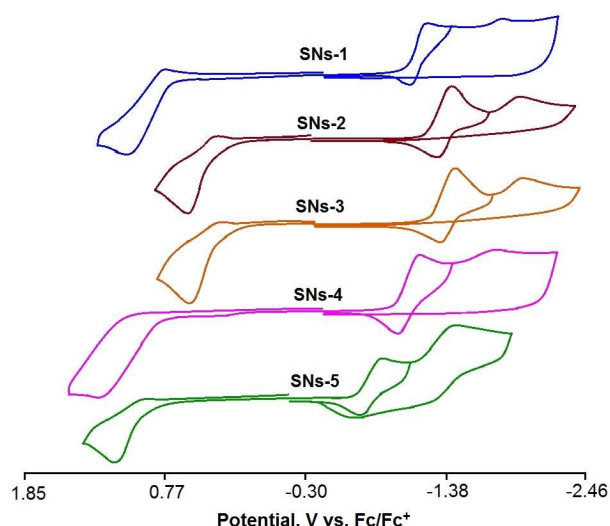


Figure 3. Cyclic voltammograms (CVs) of SNs-1(2-5) WE: CPE, CH_3CN , 10^{-1} M Bu_4NBF_4 , Potentials vs. Ag/AgCl recalculated to Fc^+/Fc .

Table 2. Redox potentials for Figure 3. Conditions: 25°C , CPE (graphite + ionic liquid + SNs-1(2-5)) as working electrode, Bu_4NBF_4 background salt, CH_3CN , 100 mV/s . Potentials vs. Fc^+/Fc , in V.

N° NPs	Oxidation			Reduction		
	Epa/Epc, V	$\Delta E_{\text{pa-c}}$, V	E1/2, V	1Epc/Epa, V	$\Delta E_{\text{pa-c}}$, V	E1/2, V
SNs-1	1.04/0.98	0.06	1.01	-1.31/-1.23	0.08	-1.27
SNs-2	0.49/0.28	0.21	0.40	-1.51/-1.44	0.07	-1.47
SNs-3	0.49/0.27	0.22	0.38	-1.51/-1.44	0.07	-1.48
SNs-4	1.09/0.98	0.11	1.04	-1.24/-1.17	0.07	-1.21
SNs-5	1.07/1.00	0.07	1.04	-1.06/-0.99	0.07	-1.03

The redox potentials for the $\text{Co}^{\text{III}}/\text{Co}^{\text{II}}$ and $\text{Co}^{\text{III}}/\text{Co}^{\text{IV}}$ redox couples of the SNs are given in Table 2.

Redox behavior of $\text{Co}^{\text{III}}(\text{bpy})_3\text{X}_3$ is well documented for various X by the easy $\text{Co}^{\text{III}}/\text{Co}^{\text{II}}$ reduction in different aprotic solutions at the potential values close to zero,^[10a-c] which is

exemplified by $E_{1/2}$ 0.05 V ref Fc^+/Fc measured for $X = \text{ClO}_4$ in CH_3CN (Figure S5). However, the oxidative behavior of the complexes within anodic range up to highest potential values is very poor documented if any. Nevertheless, the oxidation wave at +2.13 ref. Fc^+/Fc derives from the ligand-centered oxidation (Figure S5). The ESR spectrum of the complex oxidized in the acetonitrile solutions (Figure S6) is peculiar for radical-anions with $g = 2.0093$, which argues for the intraligand oxidation.

Cyclic voltammetry of $\text{Co}^{\text{III}}(\text{bpy})_3$ within SNs-1(2-5) measured in the solid state by means of the CPE technique significantly differ from those recorded in solutions of $\text{Co}^{\text{III}}(\text{bpy})_3$ complexes. In particular, the potentials of solid-state $\text{Co}^{\text{III}}/\text{Co}^{\text{II}}$ reduction are shifted on 1.0–1.4 V to the negative potential range versus the similar potentials in the solutions (Figures 3), while the reduction is reversible in both solid state and solutions.

The appearance of quasi-reversible oxidation peak at rather reasonable potential values under the solid-state oxidation of SNs-1(2-5) in CPE is rather unusual (Figure 3). The $E_{1/2}$ values of SNs-1(2-5) collected in Table 2 reveal significant effect of the nano-architecture of the composite nanoparticles on the potential values. In particular, the easiest oxidation is observed for SNs-3. It is worth noting once more the specificity of their nano-architecture derived from ultrasmall size of SNs-3 and rather high content of Co (Table 1). This is the reason for predominant interfacial localization of $\text{Co}^{\text{III}}(\text{bpy})_3$ complexes which, in turn, leads to extremely high activity of $\text{Co}^{\text{III}}(\text{bpy})_3$ complexes. It is also worth noting the super-thin silica layer onto $\text{Co}^{\text{III}}(\text{bpy})_3$ complexes as one more factor facilitating their oxidation. The oxidation potential is significantly greater for the larger nanoparticles SNs-1(4, 5), while the potential values measured for SNs-2 results from the mixture of the largest and smallest nanoparticles.

The oxidized nanoparticles produced by the preparative solid-state oxidation of SNs-1 are characterized by widened peak in the ESR spectrum with $g = 2.21$ (Figure 4), while the initial SNs-1 are EPR-silent, which is common for the lowspin $3d^6 \text{Co}^{\text{III}}$ ion ($S = 0$). The ESR spectrum also possesses the additional very widened peak which can't be accurately characterized due to its widening. It is worth noting that the

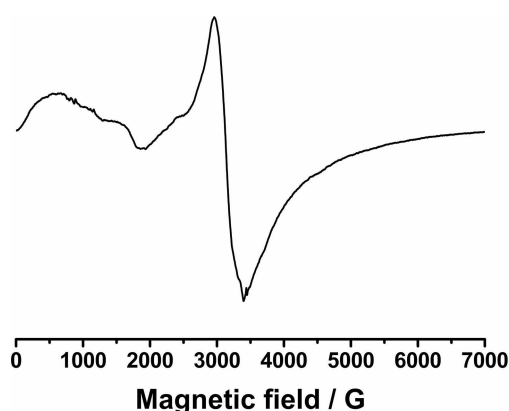


Figure 4. ESR spectrum of $[\text{Co}^{\text{IV}}(\text{bpy})_3@ \text{SiO}_2]$ NPs isolated after electrooxidation of SNs-1 at 1 V (ref. Fc^+/Fc); $g = 2.21$; $\Delta H = 450 \text{ G}$

main peak with $g=2.21$ definitely points to Co^{IV} as the result of the oxidation. However, it is rather difficult to separate between high- ($S=5/2$ or $3/2$) and low-spin Co^{IV} with $S=1/2$, since both these cases generate peak in ESR spectra.^[7b,d,g,17] The literature data demonstrate great number of high-spin $3d^5$ ions, including Mn^{II} and Fe^{III} , with $g=2.0023$, while the literature examples^[7b,d,g,17a] of low-spin Co^{IV} indicate that the latter is characterized by the g -factor significantly greater than $g=2.0023$. Thus, the main peak with $g=2.21$ derives from low-spin Co^{IV} ($S=1/2$), while in accordance with literature data^[17b] the low-field component in the ESR spectrum can be contributed by some extent of either interacting low-spin Co^{IV} ions or high-spin Co^{IV} ions.

It is worth noting that the ESR spectrum remained without any degradation within one week at least, which indicates that the nanoparticulate form exemplified by SNs-1 of the oxidized complexes provides convenient outer- and inner-sphere environment of Co^{IV} ions for their long-time stability.

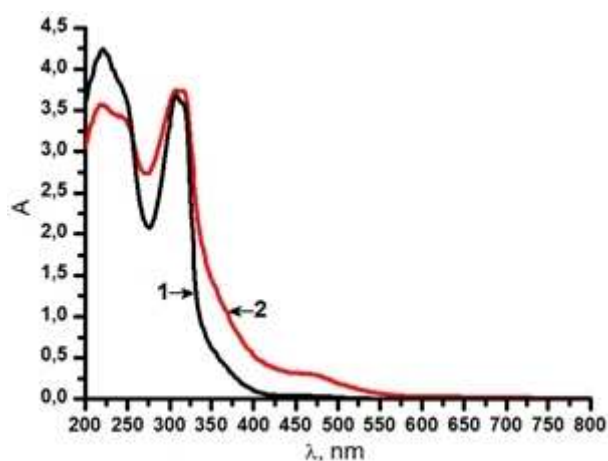


Figure 5. The solid phase absorption spectra of SNs-1 before (1) and after the solid state oxidation (2).

It is well-known that electronic absorption spectra of Co^{III} (bpy)₃ mainly derive from both intraligand and LMCT transitions, while d-d transitions will be out of the present discussion due to their low ϵ values. The energy of LMCT transitions is greatly affected by oxidation state of metal ions, thus the comparative analysis of the solid state electronic absorption spectra of SNs-1 before and after the preparative oxidation can confirm the oxidation of $\text{Co}^{\text{III/IV}}$ (bpy)₃ within the silica spheres. Indeed, the solid state electronic absorption spectra of SNs-1 recorded before and after oxidation are quite different (Figure 5).

The main spectral changes under the oxidation are manifested by the appearance of the electronic adsorption bands at longer wavelengths. The band at 475 nm and shoulder at 370 nm most probably arise from the LMCT transitions which for Co^{IV} (bpy)₃ inside the silica should be at lower energies and longer wavelengths than those for Co^{III} (bpy)₃ within SNs-1.^[7c, f, g]

3.1. Electrocatalytic Properties

Electrocatalytic properties of Co^{III} (bpy)₃ within SNs-1(3-5) as the nanocatalysts were tested in CH/NH cross-coupling reaction, exactly in the electrochemical oxidative amination of benzo-*h*-quinoline with the use of *p*-toluenesulfonamide (H_2NTs) as the aminating agent. Both benzo-*h*-quinoline and *p*-toluenesulfonamide tend to oxidize at very high potential values which are 1.52 V and 2.07 V correspondingly (Figure S7). The cyclic voltammetry of the nanocatalysts reveal catalytic current (i_{cat}) growth at the potentials of $\text{Co}^{\text{III/IV}}$ oxidation under the increasing amounts of the added *p*-toluenesulfonamide (Figure 6). The i_{cat}/i_p comes to the saturation level at the specific *p*-toluenesulfonamide : Co^{III} (bpy)₃ molar ratios which are within 16:1. Both saturation level and TOFs (turnover frequencies) calculated by means of the well-known Savéant formula^[18] depend on the architecture of the nanocatalysts. The increase in oxidation current of the catalyst in the presence of the amine

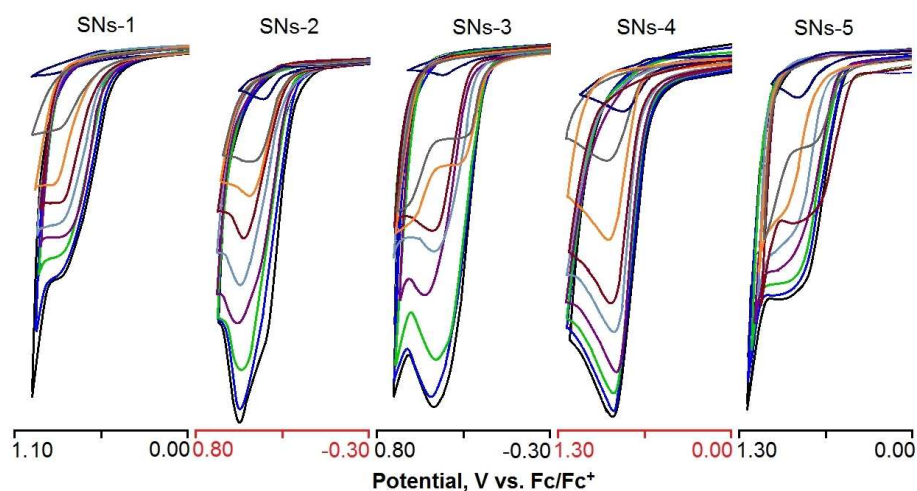


Figure 6. CVs of $[\text{Co}(\text{bpy})_3]@\text{SiO}_2$ in the absence and in the presence of increasing quantities of H_2NTs . Co: H_2NTs ratios are from 1:0 (blue) up to 1:16. (black); CPE, CH_3CN , 0.1 V s^{-1} .

is the same in both the presence and absence of the aromatic cross-coupling partner. This indicates that the coordination of the arene with the cobalt centers of the catalyst is not a rate-determining stage, while such coordination is targeted at the ligand directional selectivity of the reaction.

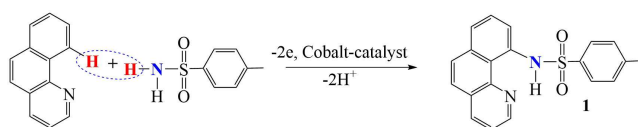
Both i_{cat}/i_p and TOF values are the most for SNs-3 (Table 3) among other nanoparticles which is rather unusual, since the oxidation potential of SNs-3 is lowest among the other nanocatalysts (Table 2). This tendency contradicts the regularities of many other electrochemical catalytic processes where the most values of k_{eff} (TOF) commonly correlate with the greatest potential values.^[18] However, the literature data introduce one example at least of inverted linear correlation between catalytic activity and formal potential of the catalyst in the electro-oxidation (or reduction).^[19] Very probably that both high rate of regeneration and greatest TOF of the SNs-3 derives from their specific nano-architecture. The specificity of the latter is manifested by the smallest size (4.5 nm) and very thin silica coating of the $Co^{III}(bpy)_3$ -based nanoprecipitates. This, in turn, provides both greatest surface activity of SNs-3 and availability of $Co^{III/IV}(bpy)_3$ complexes to the substrates, since such ultra-small size values are well-known as prerequisite for the greatest amount of the surface located complexes. This assumption is confirmed by the lowest rate of regeneration for the greatest in size nanocatalysts SNs-4 (140 nm). However, the cross-coupling selectivity is the important factor beyond the rate of regeneration which can be controlled by the nanocatalyst. The impact of the nanoparticle's architecture on the selectivity of the electrochemical oxidative amination will be discussed below.

3.2. Electrosynthesis

Screening of the nanocatalyst's efficiency in electrochemical oxidative amination of benzo-*h*-quinoline by H_2 NTs was performed at the 1:1 (substrate:amine) ratio in accordance to Scheme 2. The screening was carried out by passing of electricity (2,1 F) through the separated cell filled by the acetonitrile solution containing the components of the synthesis. The product of the synthesis was previously synthesized

Table 3. Catalytic current growths i_{cat}/i_p and corresponding TOF, s^{-1} in oxidation of H_2 NTs catalyzed by SNPs.

N° NPs	i_{cat}/i_p	TOF [s^{-1}]
SNs-1	10	3.59
SNs-2	9	2.91
SNs-3	14	7.05
SNs-4	8	2.30
SNs-5	6	1.29



Scheme 2. CH/NH cross-coupling catalyzed by $Co^{III/IV}$.

in the traditional for C–H activation multicomponent reaction conditions ($[Cp^*RhCl_2]_2$, 2,5 mol%; $AgSbF_6$, 10 mol%; $PhI(OAc)_2$, 1.5 equiv.; 60°C; 24 h) with use of Rh^{III} complex as the homogeneous catalyst.^[20] Obviously, that the synthetic protocol with the use of the nanocatalyst is much simpler: the minimum of the regenerated cobalt catalyst and the absence of specially added co-catalysts and oxidants. The conversion extents of the substrate into the product evaluated by means of 1H NMR spectral analysis of the reaction mixtures under the use of SNs-1(3–5) as the catalysts are presented in Table 4. The conversion extents are greater under the use of the nanocatalysts than for the homogeneous catalysis by $Co^{III}bpy_3(ClO_4)_3$. However, the difference between conversion extent of the substrate and the yield of the product is not the same for the nanocatalysts with different architecture (Table 4). In particular, the product yield is the least for SNs-3 becoming greater for the larger nanoparticles, although the best product yield was detected for SNs-1 which are smaller than SNs-4(5) (Table 4). Thus, there is no correlation with the size of the SNs, while the results point to the impact of the nanoparticulate architecture of SNs-3 and SNs-1 on the catalytic activity of the complexes within them.

The recyclability of the nanocatalysts was evaluated by measuring the product yields under their repeated use, as well as the leaching of the $Co^{III}(bpy)_3$ complexes after the repeated catalytic cycles. The leaching was measured by the comparative UV-Vis spectral analysis of the nanoparticles before and after the catalytic cycles (Figure S4 in SI). The spectral data reveal the insignificant leaching of the complexes after the catalytic cycle from SNs-1 (Figure S4). The leaching becomes somewhat greater for the larger nanoparticles SNs-4(5), while it is the greatest (about 35%) for the smallest ones SNs-3. The immobilized catalyst SNs-1 was tested in several reaction cycles in CH/NH cross-coupling. The results in Table 5 demonstrate the insignificant changes in the yields of product under the repeating of the reaction runs. This indicates rather high stability of the recycled catalyst, supporting a heterogeneous reaction process. After each of the rounds in Table 5, the reaction mixture was centrifuged to separate the immobilized catalyst. The nanoparticles were washed with CH_3CN , dispersed in pure CH_3CN with reagents and used directly for the next synthesis. Sevenfold use of such catalyst led only to negligible decrease in

Table 4. Electrosynthesis efficiency with different catalytic nanoparticles [$Co(bpy)_3@SiO_2$] (1 mol%) and $Co^{III}bpy_3(ClO_4)_3$ precursor (to compare). Divided cell, 2.1 F, 0.2 g (1.1 mmol) benzo-*h*-quinoline, 0.19 g (1.1 mmol) *p*-toluenesulfonamide, Co-catalyst in 15 ml CH_3CN . Electrolysis potential is 1.0 – 1.2 V ref. $Ag/AgNO_3$.

N	Catalyst	Conversion ^[a] [%]	Yield of 1 ^[b] [%]
1	SNs-1	100	90
2	SNs-2	85	50
3	SNs-3	87	51
4	SNs-4	100	70
5	SNs-5	100	72
6	$Co^{III}bpy_3(ClO_4)_3$	45	38 ^c

[a] Based on 1H NMR; [b] Isolated product; [c] Electrolysis potential is 2.05 V ref. $Ag/AgNO_3$.

Table 5. Use of recycled $[\text{Co}(\text{bpy})_2@/\text{SiO}_2]$ catalyst (1% SNs-1) ^a. Reaction conditions: Substrates ratio 1:1. $Q=2,1$ F per Bqh, -1.1 V.

Number of repeats	Total yield [%]
1	90
2	90
3	90
4	89
5	89
6	89
7	88

the products yield. After three reaction cycles no loss of the catalytic activity of the immobilized catalyst was observed.

With the optimized conditions at hand, we proceeded in exploring the scope of arenes (Table 6) with the best catalysts, SNs-1. *p*-Toluenesulfonamide as an aminating reagent was tested in electrocatalytic amination of arenes, as ligand-directed, using 2-phenylpyridine, benzo[*h*]quinoline and 1-phenylpyrazole, and also using toluene.

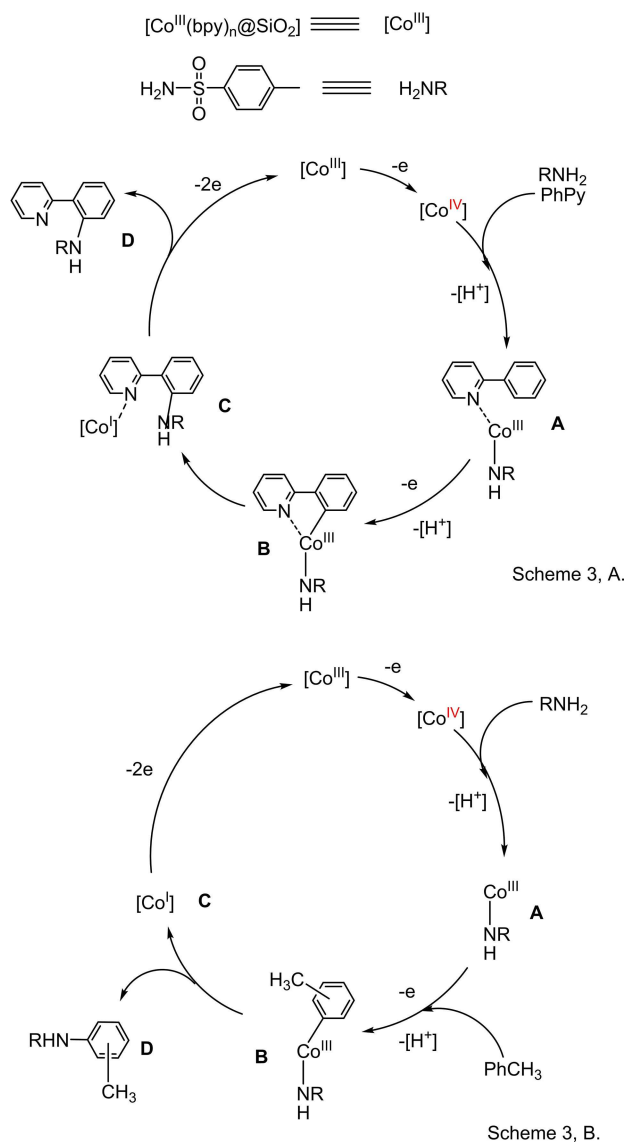
As shown in Table 6, the electrochemical approach to the amination of 2-phenylpyridine proved to be effective; the yield of the *ortho*-aminated derivative was 81%. With moderate yield (63%), 1-phenylpyrazole is also aminated under the same conditions. In the case of using toluene as the substrate, the yield of the aminated products was about 42%, but the complicated mixture of different *o*-, *m*- or *p*-substituted products was obtained in our conditions.

3.3. Mechanistic Considerations

On the basis of the experimental results and literature reports,^[21] we attempted to propose plausible reaction mechanism illustrated by Scheme 3. It is worth noting that the substitution occurs selectively into the *ortho*-position only in the case of the ligand-directed amination. Thus, the coordination of cobalt ion via the pyridine fragment of the aromatic molecule is the stage responsible for the selective *ortho*-substitution of arene (product **D** in Scheme 3,A). However, as it was previously shown, the formation of intermediate organometallic cobaltacycle with a cobalt-carbon bond is possible only for cobalt compounds in higher oxidation states^[6i,21]. Thus, the oxidation of Co^{III} catalyst to Co^{IV} at anode is the prerequisite for the coordination of Co^{IV} to 2-phenylpyridine and H_2NTs to get Co^{III} -complex **A** (Scheme 3, A). The C–H activation took place and the Co^{III} -complex **B** was formed during oxidation with

Table 6. Yields of cross-coupling product for various aromatic partners. $[\text{Co}(\text{bpy})_2@/\text{SiO}_2]$ catalyst (1% SNs-1). Reaction conditions: Substrates ratio 1:1. $Q=2,1$ F per arene, -1.1 V.

Entry	C(sp ²)-H partner	Yield of cross-coupling [%]
1	benzo- <i>h</i> -quinoline	90
2	2-phenylpyridine	81
3	1-phenylpyrazole	63
4	toluene	42 (mixture, <i>o:m:p</i>)



Scheme 3. Proposed Mechanism.

second proton loss, followed by reductive elimination from Co^{III} -complex to release the desired product and Co^{I} species **C**. Co^{I} species were re-oxidized to Co^{III} at the anode to complete the whole catalytic cycle of Co (Scheme 3, A).

Since the regeneration of Co^{III} catalyst is revealed in voltammograms even in the absence of the arene, thus, the activation of N–H bond cannot be excluded in the catalytic cycle. However, in the presence of pyridine-guiding groups in the aromatic substrate, the stage of coordination of the latter with cobalt is the key to ensure the direction of the general catalytic reaction. Moreover, both C–H and N–H bonds are activated under oxidizing conditions. For the toluene amination reaction, the coordination of cobalt with toluene without heteroatoms does not occur, however, the formation of organometallic intermediates **B** with the Co^{III} -carbon bond is possible (Scheme 3, B). However, the reaction proceeds less selectively for these clear reasons. The stages of oxidative addition and

reductive elimination of the product are also characteristic for this catalytic cycle.

4. Conclusion

Summarizing, the encapsulation of $\text{Co}^{\text{III}}(\text{bpy})_3$ complexes into silica nanoparticles by means of Stöber or water-in-oil microemulsion techniques is the facial and efficient route for synthesis of differently sized composite silica spheres as the nanocatalysts in oxidative CH/NH cross-coupling. It is also worth noting that both size and architecture of the nanoparticles provide powerful tool for modification of the oxidation potentials and catalytic activity of $\text{Co}^{\text{III}}(\text{bpy})_3$ inside the nanoparticles.

Comparative analysis of the catalytic efficiency and selectivity in the CH/NH cross-coupling highlights 50 nm sized $\text{Co}^{\text{III}}(\text{bpy})_3$ -doped silica nanoparticles synthesized by water-in-oil microemulsion technique as the most promising nanocatalyst. Very low leaching of $\text{Co}^{\text{III}}(\text{bpy})_3$ complexes from the silica matrix within the catalytic cycle along with the high product's yield is important advantage of the nanocatalyst. Easy separation of the nanoparticles after the catalytic cycle facilitates their multiple reusing. The catalytic reaction is efficient at room temperatures without the basic and/or oxidative additives commonly used in CH/NH cross-coupling. Thus, the use of Co as more cheap and abundant alternate to Rh, Pd^{II} provides high catalytic efficiency and selectivity in the oxidative C–H functionalization even at low concentrations. The developed nanocatalysts have the potential for new applications in cobalt-catalyzed carbon-heteroatom coupling or other reactions.

Experimental Section

Experimental Details see Supporting Information.

Acknowledgements

This work was supported by Russian Science Foundation grant no. 19-13-00016. The authors gratefully acknowledge the CSF-SAC FRC KSC RAS for the spectral (NMR, ESR, UV, etc.) studies.

Conflict of Interest

The authors declare no conflict of interest.

Keywords: cobalt · oxidation · supported catalysts · heterogeneous catalysis · electrochemistry

[1] Recent examples of papers on C–H activation, see: a) H. Wang, X. Gao, Z. Lv, T. Abdelilah, A. Lei, *Chem. Rev.* **2019**, *119*, 6769–6787; b) H. Kim, S. Chang, *ACS Catal.* **2016**, *6*, 2341–2351; c) J. Jiao, K. Murakami, K. Itami, *ACS Catal.* **2016**, *6*, 610–633; d) P. Kalck, M. Urrutigoity, *Chem. Rev.* **2018**,

- 118, 3833–3861; e) M. D. Kärkäs, *Chem. Soc. Rev.* **2018**, *47*, 5786–5865; f) N. Sauer mann, T. H. Meyer, Y. I. Qiu, L. Ackermann, *ACS Catal.* **2018**, *8*, 7086–7103; g) T. H. Meyer, L. H. Finger, P. Gandee pan, L. Ackermann, *Trends in Chemistry* **2019**, *1*, 63–76; h) L. Zhang, L. Liardet, J. Luo, D. Ren, M. Grätzel, X. Hu, *Nature Catalysis* **2019**, *2*, 366–373; i) P. Gandee pan, T. Müller, D. Zell, G. Cera, S. Warratz, L. Ackermann, *Chem. Rev.* **2019**, *119*, 2192–2452; j) G. Pototschnig, N. Maulide, M. Schnürch, *Chem. Eur. J.* **2017**, *23*, 1–28; k) M. Usman, Z.-H. Ren, Y.-Y. Wang, Z.-H. Guan, *Synthesis*. **2017**, *49*, 1419–1443; l) M. Moselage, J. Li, L. Ackermann, *ACS Catal.* **2016**, *6*, 498–525.
- [2] a) H. Tian, X. Li, L. Zeng, J. Gong, *ACS Catal.* **2015**, *58*, 4959–4977; b) M. Yadav, R. K. Sharma, *Curr Opin Green Sustain Chem.* **2019**, *15*, 47–59; c) M. N. Khrizanforov, S. V. Fedorenko, S. O. Strelkalova, K. V. Kholod, A. R. Mustafina, M. Y. Zhilkin, V. V. Khrizanforova, Y. N. Osin, V. V. Salnikov, T. V. Gryaznova, Y. H. Budnikova, *Dalton Trans.* **2016**, *45*, 11976–11982; d) P. Ryabchuk, G. Agostini, M.-M. Pohl, H. Lund, A. Agapova, H. Junge, K. Junge, M. Beller, *Sci. Adv.* **2018**, *4*, eaat0761; e) Y. B. Dudkina, T. V. Gryaznova, Y. N. Osin, V. V. Salnikov, N. A. Davydov, S. V. Fedorenko, A. R. Mustafina, D. A. Vivic, O. G. Sinyashin, Y. H. Budnikova, *Dalton Trans.* **2015**, *44*, 8833–8838. f) P. Sarmah, R. Chakrabarty, P. Phukan, B. K. Das, *J.Mol. Catalysis A: Chemical* **2007**, *268*, 36–44.
- [3] a) Z. Wan, Q. Xu, H. Li, Y. Zhang, Y. Ding, J. Wang, Z. Wana, T. Zhou, Y. Du, S. Yin, X. Tian, H. Yang, X. Wang, B. Liu, H. Zheng, S. Qiao, R. Xu, *Energy Environ. Sci.* **2016**, *9*, 2563; b) P. Zhou, L. Jiang, F. Wang, K. Deng, K. Lv, Z. Zhang, *Sci. Adv.* **2017**, *3*, e1601945; c) J. Sun, J. Yu, Q. Ma, F. Meng, X. Wei, Y. Sun, N. Tsubaki, *Sci. Adv.* **2018**, *4*, eaau3275; d) M. Colella, C. Carlucci, R. Luisi, *Top. Curr. Chem.* **2018**, *376*, 46; e) L. Liu, A. Corma, *Chem. Rev.* **2018**, *118*, 4981–5079; f) D. Wang, D. Astruc, *Chem. Soc. Rev.* **2017**, *46*, 816–854; g) R. K. Sharma, S. Sharma, S. Dutta, R. Zboril, M. B. Gawande, *Green Chem.* **2015**, *17*, 3207–3230; h) Effects of Nanoconfinement on Catalysis, Edited by Rinaldo Poli. Springer International Publishing, **2017**. 266 pp.
- [4] a) J. Miao, H. Ge, *Eur. J. Org. Chem.* **2015**, 7859–7868; b) W.-H. Rao, B.-F. Shi, *Org. Chem. Front.* **2016**, *3*, 1028–1047.
- [5] T. K. Hyster, *Catal. Lett.* **2015**, *145*, 458–467.
- [6] a) N. Yoshikai, *ChemCatChem.* **2015**, *7*, 732–734; b) D. Wei, X. Zhu, J.-L. Niu, M.-P. Song, *ChemCatChem.* **2016**, *8*, 1242–1263; c) J. Sanjosé-Orduna, D. Gallego, A. Garcia-Roca, E. Martin, J. Benet-Buchholz, M. H. Pérez-Temprano, *Angew. Chem. Int. Ed.* **2017**, *56*, 12137–12141; *Angew. Chem.* **2017**, *129*, 12305–12309; d) M. Usman, Z.-H. Ren, Y.-Y. Wang, Z.-H. Guan, *Synthesis*, **2017**, *49*, 1419–1443; e) S. Wang, S.-Y. Chen, X.-Q. Yu, *Commun. Chem.* **2017**, *53*, 3165–3180; f) T. Yoshino, S. Matsunaga, *Adv. Synth. Catal.* **2017**, *359*, 1245–1262; g) M. Pengchen, H. Chen, *ACS Catal.* **2019**, 1962–1972; h) T. Yoshino, H. Ikemoto, S. Matsunaga, M. A. Kanai, *Angew. Chem. Int. Ed.* **2013**, *52*, 2207–2211; *Angew. Chem.* **2013**, *125*, 2263–2267; i) X. Wu, K. Yang, Y. Zhao, H. Sun, G. Li, H. Ge, *Nat. Commun.* **2015**, *6*, 6462–6471; j) L. Grigorjeva, O. Daugulis, *Angew. Chem. Int. Ed.* **2014**, *53*, 10209–10212; *Angew. Chem.* **2014**, *126*, 10373–10376. k) Y. Komagalla, N. Chatani, *Coord. Chem. Rev.* **2017**, *350*, 117–135; l) G. Rouquet, N. Chatani, *Angew. Chem. Int. Ed.* **2013**, *52*, 11726–11743; *Angew. Chem.* **2013**, *125*, 11942–11959; m) Y. Baek, T. A. Betley, *J. Am. Chem. Soc.* **2019**, *141*, 7797–7806.
- [7] a) K. Dimitrou, A. D. Brown, T. E. Concolino, A. L. Rheingold, G. Christou, *Chem. Commun.* **2001**, 1284–1285; b) J. G. McAlpin, T. A. Stich, C. A. Ohlin, Y. Surendranath, D. G. Nocera, W. H. Casey, R. D. Britt, *J. Am. Chem. Soc.* **2011**, *133*, 39,15444–15452; c) F. F. Pfaff, S. Kundu, M. Risch, S. Pandian, F. Heims, I. Pryjomskaya-Ray, P. Haack, R. Metzinger, E. Bill, H. Dau, P. Comba, K. Ray, *Angew. Chem. Int. Ed.* **2011**, *50*, 1711–1715; *Angew. Chem.* **2011**, *123*, 1749–1753; d) S. Hong, F. F. Pfaff, E. Kwon, Y. Wang, M.-S. Seo, E. Bill, K. Ray, W. Nam, *Angew. Chem. Int. Ed.* **2014**, *53*, 10403–10407; *Angew. Chem.* **2014**, *126*, 10571–10575; e) D. Das, S. Pattanayak, K. K. Singh, B. Garaib, S. S. Gupta, *Chem. Commun.* **2016**, *52*, 11787–11790; f) C. N. Brodskya, R. G. Hadt, D. Hayes, B. J. Reinhart, N. Lia, L. X. Chen, D. G. Nocera, *PNAS* **2017**, *114*, 3855–3860; g) B. Wang, Y.-M. Lee, W.-Y. Tcho, S. Tussupbayev, S.-Tae Kim, Y. Kim, M. S. Seo, K.-B. Cho, Y. Dede, B. C. Keegan, T. Ogura, S. H. Kim, T. Ohta, M.-H. Baik, K. Ray, J. Shearer, W. Nam, *Nature Comm.* **2017**, *8*, 14839; h) L. Zhang, Y. Liu, L. Deng, *J. Am. Chem. Soc.* **2014**, *136*, 15525–15528; i) Y. Baek, T. A. Betley, *J. Am. Chem. Soc.*, Just Accepted Manuscript, DOI: 10.1021/jacs.9b01262; j) R. G. Hadt, D. Hayes, C. N. Brodsky, A. M. Ullman, D. M. Casa, M. H. Upton, D. G. Nocera, L. X. Chen, *J. Am. Chem. Soc.* **2016**, *138*, 11017–11030.
- [8] a) L. Zhang, Y. Liu, L. Deng, *J. Am. Chem. Soc.* **2014**, *136*, 15525–15528; b) Q. Zhang, A. Bell-Taylor, F. M. Bronston, J. D. Gorden, C. R. Goldsmith, *Inorg. Chem.* **2017**, *56*, 773–782.

- [9] a) R. P. Bagwe, C. Yang, L. R. Hilliard, W. Tan, *Langmuir*, **2004**, *20*, 8336–8342; b) W. Stöber, A. Fink, E. Bohn, *J. Colloid Interface Sci.* **1968**, *26*, 62–69; c) D. Zhang, Z. Wu, J. Xu, J. Liang, J. Li, W. Yang, *Langmuir* **2010**, *26*, 6657–6662; d) M. N. Khrizanforov, S. V. Fedorenko, A. R. Mustafina, V. V. Khrizanforova, K. V. Kholin, T. V. Gryaznova, V. V. Grinenko, Y. H. Budnikova *RCS Adv.* **2019**, *9*, 22627–22635; e) A. R. Mustafina, S. V. Fedorenko, O. D. Konovalova, A. Yu. Menshikova, N. N. Shevchenko, S. E. Soloveva, A. I. Konovalov, I. S. Antipin, *Langmuir* **2009**, *25*, 3146–3151.
- [10] a) H. Ferreira, M. M. Conradie, J. Conradie, *Data in Brief* **2019**, *22*, 436–445; b) H. Ferreira, M. M. Conradie, J. Conradie, *Inorg. Chim. Acta* **2019**, *486*, 26–35; c) Y. Katayama, S. Nakayama, N. Tachikawa, K. Yoshii, *J. Electrochem. Soc.* **2017**, *164*, H5286–H5291; d) S. Margel, W. Smith, F. C. Anson, *J. Electrochem. Soc.: Electrochem. Sci. Technology*, **1978**, 241–246; e) J. M. Rao, M. C. Hughes, D. J. Macero, *Inorg. Chim. Acta*, **1979**, *35*, L369–L373; f) R. S. Gaddie, C. B. Moss, C. M. Elliott, *Langmuir* **2013**, *29*, 825–831; g) P. T. Selvi, M. Palaniandavar, *Inorg. Chim. Acta* **2002**, *337*, 420–428; h) S. Aroua, T. K. Todorova, P. Hommes, L.-M. Chamoreau, H.-U. Reissig, V. Mougél, M. Fontecave, *Inorg. Chem.* **2017**, *56*, 5930–5940; i) L. Polleux, E. Labbé, O. Buriac, J. Périchon, *Chem. Eur. J.* **2005**, *11*, 4678–4686; j) Y. G. Budnikova, A. G. Kafiyatullina, Y. M. Kargin, O. G. Sinyashin, *Russ. J. Gen. Chem.* **2001**, *71*, 231–233; k) Y. G. Budnikova, A. G. Kafiyatullina, Y. M. Kargin, O. G. Sinyashin, *Russ. Chem. Bull.* **2002**, *51*, 1702–1708.
- [11] a) W. Xiao-Ying, Y. Wen, Z. Jing-Ming, D. Ping, H. Pin-Gang, F. Yu-Zhi, *Chin. J. Chem.* **2008**, *26*, 315–320; b) L. Qian, X. Yang, *Adv. Funct. Mater.* **2007**, *17*, 1353–1358; c) H. Li, Y. Mu, J. Lu, W. Wei, Y. Wan, S. Liu, *Analyt. Chem.* **2014**, *86*, 3602–3609; d) E. Besic Gyenge, X. Darphin, A. Wirth, U. Pieleh, H. Walt, M. Bredell, C. Maake, *J. Nanobiotechnol.*, **2011**, *9*, 32; e) S. R. Kandibanda, N. Gundelboina, S. Das, V. M. Sunkara, *J. Photochem. Photobiol. B: Biology*, **2018**, *178*, 270–276; f) S. Santoro, V. Sebastian, A. J. Moro, C. A. M. Portugal, J. C. Lima, I. M. Coelho, J. G. Crespo, R. Mallada, *J. Colloid Interface Sci.*, **2017**, *486*, 144–152; g) M. Mirenda, V. Levi, M. L. Bossi, L. Bruno, A. V. Bordoni, A. E. Regazzoni, A. Wolosiuk, *J. Colloid Interface Sci.* **2013**, *392*, 96–101.
- [12] a) N. Zhu, H. Cai, P. He, Y. Fang, *Anal. Chim. Acta*, **2003**, *481*, 181–189; b) T. N. Yakubovich, N. I. Ermokhina, Y. I. Bratushko, Y. L. Zuba, A. A. Chuiko, *Dioxygen Activation and Homogeneous Catalytic Oxidation*, **1991**, 66, Elsevier Science Publishers B. V. Amsterdam, p. 179–188.
- [13] a) R. Trujillano, J.-F. Lambert, C. Louis, *J. Phys. Chem. C*, **2008**, *112*, 18551–18558; b) S. A. Ranaweera, M. D. Rowe, K. B. Walters, W. P. Henry, M. G. White, J. M. Rodriguez, *App. Catalysis A: General*, **2017**, *529*, 108–117; c) F. Rajabi, R. Luque, J. H. Clark, B. Karimi, D. J. Macquarrie, *Catalysis Comm.* **2011**, *12*, 510–513; d) L. Chen, B.-D. Li, Q.-X. Xu, D.-B. Liu, *Chin. Chem. Lett.* **2013**, *24*, 849–852; e) R. Antony, S. T. D. Manickam, S. Balakumar, *J. Inorg. Organomet. Polym.* **2017**, *27*, 418–426; f) G. Di Carlo, M. Luaidi, A. M. Venezia, M. Boutonnet, M. Sanchez-Dominguez, *Catalysts* **2015**, *5*, 442–459; g) M. Wolf, E. K. Gibson, E. J. Olivier, J. H. Neethling, C. R. A. Catlow, N. Fischer, M. Claeys, *Catalysis Today*, in press.
- [14] a) S. Fedorenko, D. Gilmanova, A. Mukhametshina, I. Nizameev, K. Kholin, B. Akhmadeev, A. Voloshina, A. Sapunova, S. Kuznetsova, A. Daminova, S. Katsyuba, R. Zairov, A. Mustafina, *J. Materials Science*, **2019**, *54*, 9140–9154; b) S. V. Fedorenko, S. L. Grechikina, A. R. Mustafina, K. V. Kholin, A. S. Stepanov, I. R. Nizameev, I. E. Ismaev, M. K. Kadirov, R. R. Zairov, A. N. Fattakhova, R. R. Amirov, S. E. Soloveva, *Colloids Surf. B* **2017**, *149*, 243–249.
- [15] M. Mirenda, V. Levi, M. L. Bossi, L. Bruno, A. V. Bordoni, A. E. Regazzoni, A. Wolosiuk, *J. Colloid Interface Sci.* **2013**, *392*, 96–101.
- [16] a) M. N. Khrizanforov, D. M. Arkhipova, R. P. Shekurov, T. P. Gerasimova, V. V. Ermolaev, D. R. Islamov, V. A. Miluykov, O. N. Kataeva, V. V. Khrizanforova, O. G. Sinyashin, Y. H. Budnikova, *J. Solid State Electrochem.* **2015**, *19*, 2883; b) T. Gryaznova, Y. Dudkina, M. Khrizanforov, O. Sinyashin, O. Kataeva, Y. Budnikova, *J. Solid State Electrochem.* **2015**, *19*, 2665; c) R. Shekurov, V. Khrizanforova, L. Gilmanova, M. Khrizanforov, V. Miluykov, O. Kataeva, Z. Yamaleeva, T. Burganov, T. Gerasimova, A. Khamatgalimov, S. Katsyuba, V. Kovalenko, Y. Krupskaya, V. Kataev, B. Büchner, V. Bon, I. Senkovska, S. Kaskel, A. Gubaidullin, O. Sinyashin, Y. Budnikova, *Dalton Trans.* **2019**, *48*, 3601–3609; d) M. N. Khrizanforov, S. V. Fedorenko, A. R. Mustafina, K. V. Kholin, I. R. Nizameev, S. O. Strekalova, V. V. Grinenko, T. V. Gryaznova, R. R. Zairov, R. Mazzaro, V. Morandi, A. Vomiero, Y. H. Budnikova, *Dalton Trans.* **2018**, *47*, 9608–9616.
- [17] a) S. A. Warda, W. Massa, D. Reinen, Z. Hu, G. Kaindl, F. M. de Groot, *J. Solid State Chem.* **1999**, *146*, 79–87; b) J. G. McAlpin, Y. Surendranath, M. Dinca, T. A. Stich, S. A. Stoian, W. H. Casey, R. D. Britt, *J. Am. Chem. Soc.* **2010**, *132*, 6882–6883; c) E. M. Zolnhofer, M. Käß, M. M. Khusniyarov, F. W. Heinemann, L. Maron, M. van Gastel, E. Bill, K. Meyer, *J. Am. Chem. Soc.* **2014**, *136*, 15072–15078.
- [18] a) E. S. Rountree, B. D. McCarthy, T. T. Eisenhart, J. L. Dempsey, *Inorg. Chem.* **2014**, *53*, 9983–10002; b) C. Costentin, J.-M. Savéant, *ChemElectroChem* **2014**, *1*, 1226–1236.
- [19] C. Gutierrez, J. Francisco, S. J. Pavez, F. Bedioui, J. H. Zagal, *Electrocatalysis* **2012**, *3*, 153–159.
- [20] H. Zhao, Y. Shang, W. Su, *Org. Lett.*, **2013**, *15*, 5106–5109.
- [21] a) S. Maity, R. Kancherla, U. Dhawa, E. Hoque, S. Pimparkar, D. Maiti, *ACS Catal.* **2016**, *68*, 5493–5499; b) X. Gao, P. Wang, L. Zeng, S. Tang, A. Lei, *J. Am. Chem. Soc.* **2018**, *140*, 4195–4199; c) O. Planas, P. G. Chirila, C. J. Whiteoak, X. Ribas, *Advances in Organometallic Chemistry*, Vol. 69, ch.4. (Ed.: P. J. Pérez), Elsevier Inc., **2018**, pp.209–282.

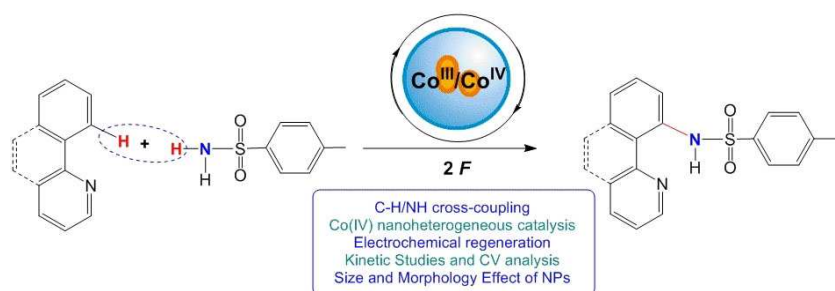
Manuscript received: July 30, 2019

Revised manuscript received: September 2, 2019

Accepted manuscript online: September 3, 2019

Version of record online: ■■■, ■■■■

FULL PAPERS



Don't get cross, get coupling! Co^{IV} species prepared by electrooxidation of $\text{Co}^{\text{III}}(\text{bpy})_3$ -doped silica nanoparticles (SNs) at relatively low anodic potentials have demonstrated high catalytic activity. Both size and architecture of the SNs are highlighted as

the factors beyond the complex structure affecting its oxidation potential and catalytic efficiency. These factors have been optimized for a catalyst with high efficiency, easy separation and reusability.

Prof. Dr. Y. Budnikova*, Dr. O. Bochkova, Dr. M. Khrizanforov, Dr. I. Nizameev, Dr. K. Kholin, Dr. T. Gryaznova, A. Laskin, Y. Dudkina, Dr. S. Strekalova, Dr. S. Fedorenko, A. Kononov, Prof. Dr. A. Mustafina

1 – 11

Selective $\text{C}(\text{sp}^2)\text{-H}$ Amination Catalyzed by High-Valent Cobalt (III)/(IV)-bpy Complex Immobilized on Silica Nanoparticles